Midinfrared surface-plasmon resonance: A novel biophysical tool for studying living cells

M. Golosovsky,[1,a)] V. Lirtsman,[1] V. Yashunsky,[1] D. Davidov,[1] and B. Aroeti[2]

[1]*The Racah Institute of Physics, The Hebrew University of Jerusalem, 91904 Jerusalem, Israel*
[2]*Department of Cell and Animal Biology, The Alexander Silberman Institute of Life Sciences, The Hebrew University of Jerusalem, 91904 Jerusalem, Israel*

We discuss the surface-plasmon resonance (SPR) technique based on Fourier transform infrared (FTIR) spectrometry. We explore the potential of the infrared surface plasmon technique for biological studies in aqueous solutions and compare it with the conventional surface plasmon technique operating in the visible range. We demonstrate that the sensitivity of the SPR technique in the infrared range is not lower and in fact is even higher. We show several examples of applying FTIR-SPR for biological studies: (i) monitoring D-glucose concentration in solution and (ii) measuring D-glucose uptake by erythrocytes in suspension. We emphasize the advantages of infrared SPR for studying living cell cultures and show how this technique can be used for characterization of (i) cholesterol penetration into plasma membrane and (ii) transferrin-induced clathrin-mediated endocytosis. © *2009 American Institute of Physics*. [DOI: 10.1063/1.3116143]

I. GENERAL INTRODUCTION

Surface plasmon resonance (SPR) is the resonant excitation of the surface electromagnetic wave propagating at the metal-dielectric interface.[1–3] This technique has become an important research tool in biophysics. The interest in it has been spurred by its potential for biosensing, the appearance of commercial instruments, and the general interest in plasmonics.[4] The SPR technique measures the refractive index or optical absorption with high sensitivity and is particularly advantageous for biosensing since (i) it is a label-free method[5] and (ii) it can monitor the kinetics of biological processes in real time. Several overviews summarize SPR applications in biology and biochemistry.[6–14] In particular, SPR in the visible range has been used to study membranes[15–22] and cell cultures.[23–26] The SPR technique has been used in several modalities such as SPR-enhanced fluorescence,[27] SPR imaging,[3,28] and SPR spectroscopy.[29–32]

The majority of the SPR applications use laser sources operating in the visible range. Recently, several SPR techniques operating in the near-infrared (NIR) range appeared,[33–38] some of which use a Fourier transform IR (FTIR) spectrometer as a light source.[39–42] In contrast with the conventional SPR technique that operates with a laser source and employs angular interrogation, the FTIR-SPR technique operates with a continuum wavelength source and employs wavelength interrogation. So far, FTIR-SPR techniques utilized glass-based optics that limited its operation to the NIR range. We extended the FTIR-SPR technique to the mid-IR range using a ZnS prism.[43,44] We found that new opportunities are offered by this technique.

- *High sensitivity*. Since conductive losses in the IR range are lower than those in the visible range, the IR SPR can be more sensitive than its visible range counterpart.
- *Penetration depth* of the surface plasmon (SP) in the visible range is very short. This is beneficial for studying very thin layers, but detrimental for studying cells and cell cultures. The IR SP penetrates much deeper and is more appropriate for studying cells.
- *Fast multiwavelength measurements*. The ability to detect SPR at varying wavelengths and/or varying angles allows "tuning" the SPR to any desired spectral range in order to achieve high sensitivity and appropriate penetration depth.
- *Spectroscopy*. Since many biomolecules have specific absorption bands in the IR range ("fingerprints"), performing multiwavelength SPR measurements in the spectral range of fingerprints, in principle, allows these biomolecules to be identified selectively.

Next, we will analyze the SPR in the IR and identify those niches where it is especially useful for biosensing. Thereafter, we will discuss several FTIR-SPR applications developed in our group.

II. THEORETICAL INTRODUCTION

A. Surface plasmon definition

SP is an electromagnetic wave $\mathbf{E}_{sp} = \mathbf{E}_0 e^{-ik_x x - k_z z}$ that propagates along the metal-dielectric interface and exponentially decays in the perpendicular direction.[1–3] The SP dispersion relations in the dielectric and in the metal are correspondingly

$$k_x^2 - k_{zd}^2 = \epsilon_d k_0^2, \tag{1}$$

$$k_x^2 - k_{zm}^2 = \epsilon_m k_0^2. \tag{2}$$

Here, k_0 is the wave vector in free space and ϵ_m and ϵ_d are the complex dielectric permittivities of the metal and of the

---

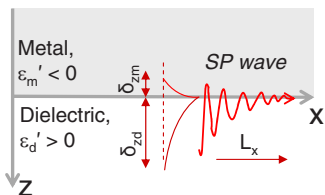a)Electronic mail: golos@vms.huji.ac.il.

FIG. 1. (Color online) Schematic of the SP propagating at the metal-dielectric interface. δ_{zm} and δ_{zd} are penetration depths into metal and dielectric media, correspondingly. L_x is the lateral propagation length that is determined by conductive, dielectric, and radiation losses.

dielectric, correspondingly, where $\epsilon'_m < 0$. When the SP propagates along the interface between two unbounded media (Fig. 1), its wave vector is

$$k'_x + ik''_x = k_0 \left(\frac{\epsilon_m \epsilon_d}{\epsilon_m + \epsilon_d} \right)^{1/2}. \tag{3}$$

SP is a TM wave. The ratio of the longitudinal and the transverse field components is $|E_z/E_x| = \sqrt{\epsilon_d/|\epsilon_m|}$ in the dielectric medium and $|E_z/E_x| = \sqrt{|\epsilon_m|/\epsilon_d}$ in the metal.

B. Surface plasmon excitation: Kretschmann's geometry

Because of the limited penetration of the SP wave into the dielectric medium, it is widely used in monitoring the refractive index of thin dielectric layers. The most widely used Kretschmann excitation geometry includes a high-refractive-index prism, a thin metal film, and a dielectric medium in contact with this film (Fig. 2). The reflectivity as a function of the incident angle (or wavelength) exhibits a sharp minimum at a certain angle Θ_{sp} corresponding to the SP excitation.[6] By measuring the resonant angle/wavelength, one can determine the refractive index of the dielectric medium with high accuracy. The sensitivity of this technique is limited by the angular width of the SPR, $\Delta\Theta_{sp}$. Next, we will develop compact expressions for the SPR angle and width, Θ_{sp}, $\Delta\Theta_{sp}$
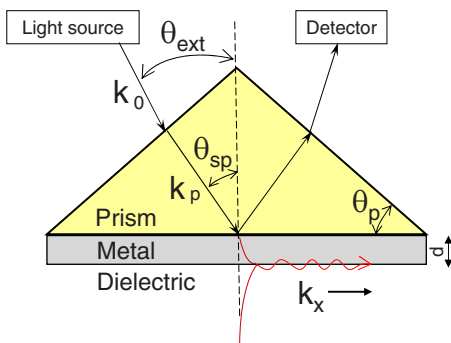
The resonance condition is

FIG. 2. (Color online) Kretschmann geometry of the SP excitation in the attenuated total reflection regime using a high-refractive-index prism and a thin metal film. k_0 and k_p are wave vectors in free space and in the prism. k_x is the SP wave vector. Θ_{sp} is the angle of incidence at the prism/metal/dielectric interface that corresponds to the resonant excitation of the SP. Θ_p is the angle at the base of the prism and Θ_{ext} is the external angle that is determined by Θ_{sp} and by the prism material and shape. Upon proper choice of the metal film thickness d, the resonance reflectivity approaches zero and the off-resonance reflectivity approaches unity.
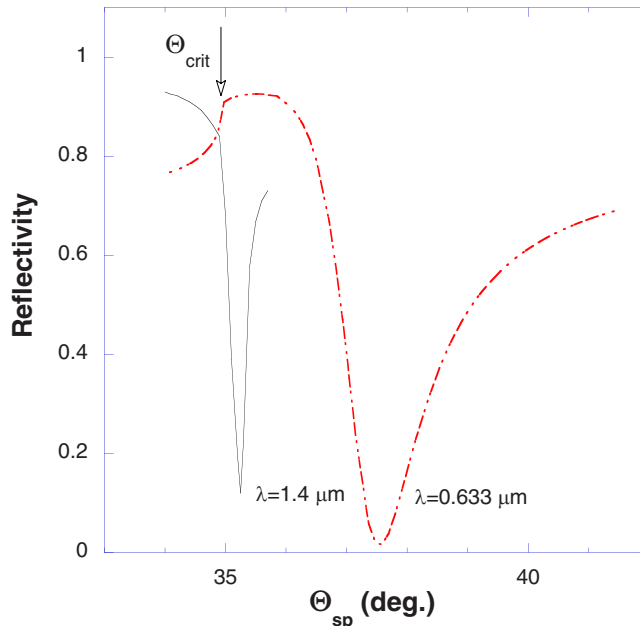

FIG. 3. (Color online) SPR at the Au/air interface. The SPR in the visible range was excited using a He–Ne laser and a 60° SF-10 prism coated with a 47-nm-thick Au film. The SPR in the IR range was excited using an FTIR spectrometer and an SF-11 right-angle prism coated with a 30.4-nm-thick Au film. Note the wide SPR in the visible range ($\lambda = 0.633$ μm) and the sharp resonance in the IR ($\lambda = 1.4$ μm). The SPR in the visible range is well displaced with respect to the critical angle whereas the SPR in the IR range is very close to the critical angle.

$$k_x = k_p \sin \Theta_{sp}, \tag{4}$$

where n_p is the refractive index and $k_p = n_p k_0$ is the wave vector in the prism. Equations (3) and (4) yield the resonant angle

$$\sin \Theta_{sp} = \frac{1}{n_p} \left(\frac{\epsilon_m \epsilon_d}{\epsilon_m + \epsilon_d} \right)^{1/2}. \tag{5}$$

This angle always exceeds the critical angle

$$\sin \Theta_{cr} = \frac{\epsilon_d^{1/2}}{n_p}. \tag{6}$$

To recast these expressions using an external angle (see Fig. 2), we apply Snell's law and obtain

$$\sin(\Theta_{ext} - \Theta_p) = n_p \sin(\Theta_{sp} - \Theta_p), \tag{7}$$

where Θ_{sp} is the angle at the base of the prism (Fig. 2). Figure 3 compares the SPR in the visible ($\lambda = 0.633$ μm) and in the IR ($\lambda = 1.4$ μm) range. The SPR appears as a pronounced reflectivity dip. In the visible range, this dip is wide and appears well above the critical angle, whereas in the IR range, this dip is very narrow and is very close to the critical angle.

The depth of the SPR in Kretschmann geometry is fine tuned by the careful choice of the metal film thickness, d. Note that the SP propagating along a thin metal film is not a true surface wave but rather a leaky wave that radiates a considerable part of its energy back into the prism.[1,45] For the optimal metal film thickness, the reflectivity at the resonant angle achieves its minimum value and approaches zero (the so-called critical coupling regime), whereas radiation

losses are equal to intrinsic losses: ϵ_m'', ϵ_d''. The radiation affects the SP dispersion relation [Eq. (3)] as well. The resonant angle [Eq. (5)] is slightly shifted by $1°–1.5°$, whereas k_x'' is changed more significantly; in the critical coupling regime it increases by a factor of 2 with respect to that given by Eq. (3).[45]

C. IR surface plasmon resonance propagating along a thin metal film: Modeling

Since we focus on the biological applications of the SPR, we will next consider only water-based samples. We will assume that the metal film is composed of gold and that its thickness is optimal, i.e., it corresponds to the critical coupling regime. Since the dielectric constant of gold at IR frequencies is very high, $\epsilon_m' \gg \epsilon_d \sim 1$, conductor losses are small, $\epsilon_m''/\epsilon_m' \ll 1$. If the dielectric losses are also small, then $\epsilon_d''/\epsilon_d' \ll 1$, then $k_x' \gg k_x''$. Under these conditions, we obtain useful expressions for the real and imaginary parts of the SP wave vector

$$k_x' \approx k_0 \left(\frac{\epsilon_m' \epsilon_d'}{\epsilon_m' + \epsilon_d'} \right)^{1/2} \qquad (8)$$

$$k_x'' \approx k_0 \left(\frac{\epsilon_m' \epsilon_d'}{\epsilon_m' + \epsilon_d'} \right)^{3/2} \left(\frac{\epsilon_d''}{\epsilon_d'^2} + \frac{\epsilon_m''}{\epsilon_m'^2} \right) \qquad (9)$$

$$k_{zm} = k_0 \left(\frac{\epsilon_m^2}{-\epsilon_m - \epsilon_d} \right)^{1/2} \qquad (10)$$

$$k_{zd} = k_0 \left(\frac{\epsilon_d^2}{-\epsilon_m - \epsilon_d} \right)^{1/2} \qquad (11)$$

(Note that $\epsilon_m' < 0$.) The SP penetration depth into the dielectric is

$$\delta_{zd} = \frac{1}{2k_{zd}} = \frac{\lambda_0}{4\pi} \left(\frac{-\epsilon_m' - \epsilon_d'}{\epsilon_d'^2} \right)^{1/2} \qquad (12)$$

The SP propagation length along the metal-dielectric interface is[1,45]

$$L_x = \frac{1}{2k_x''} = \frac{\lambda_0}{4\pi} \left(\frac{\epsilon_m' + \epsilon_d'}{\epsilon_m' \epsilon_d'} \right)^{3/2} \left(\frac{\epsilon_d''}{\epsilon_d'^2} + \frac{\epsilon_m''}{\epsilon_m'^2} \right)^{-1} \qquad (13)$$

Since the dielectric constant of the metal in the IR range is very high, $|\epsilon_m'| \gg 1$, then $\epsilon_m''/\epsilon_m'^2 \ll 1$ (this is valid even if the loss tangent of the metal is high, $\epsilon_m''/|\epsilon_m'| \sim 1$). Therefore, the conductor loss contribution to L_x is negligible and is determined mainly by the dielectric loss.

To estimate the SPR width $\Delta\Theta_{sp}$ we noted that Eq. (4) yields $\delta k_x = \cos \Theta_{sp} \delta\Theta_{sp}$. We replaced there δk_x by k_x'' and found

$$\Delta\Theta_{sp} = A \frac{k_x''}{k_p \cos \Theta_{sp}}, \qquad (14)$$

where A is a numerical constant that depends on how the SPR width is defined (full width at half maximum or differently). Using Eqs. (7) and (14), we obtain

$$\Delta\Theta_{ext} = A \frac{\cos(\Theta_p - \Theta_{sp})}{\cos(\Theta_p - \Theta_{ext}) \cos \Theta_{sp}} \frac{k_x''}{k_0}. \qquad (15)$$

For realistic parameters of the prism and the sample ($n_p = 2–2.3$, $\Theta_p = 45°$, $n_d = 1.25–1.45$), the angular dependence of the prefactor, $\cos(\Theta_p - \Theta_{sp})/\cos(\Theta_p - \Theta_{ext})\cos \Theta_{sp}$, is very weak and can be replaced by a numerical constant. Using Eq. (9), we recast Eq. (15) as follows:

$$\Delta\Theta_{ext} \approx \tilde{A} \epsilon_d^{3/2} \left(\frac{\epsilon_m''}{\epsilon_m'^2} + \frac{\epsilon_d''}{\epsilon_d'^2} \right), \qquad (16)$$

where $\tilde{A}$ absorbs all numerical constants. A comparison of the exact numerical calculations for the ZnS prism and water as a dielectric medium yields $\tilde{A} = 1.85$. An approximate expression for the SPR width is

$$\Delta\Theta = \sqrt{\Delta\Theta_{ext}^2 + \Delta\Theta_{div}^2}, \qquad (17)$$

where $\Delta\Theta_{div}$ is the incident beam divergence. Although the SPR width can be calculated exactly using Fresnel reflectivity formulae, Eqs. (16) and (17) are more amenable to analysis.

The SPR width is a crucial factor that determines the sensitivity of the SPR technique. The latter is usually[6,45] defined as $\partial R/\partial n$, where R is the reflectivity and $n = \epsilon_d^{1/2}$. After recasting this expression using an angular variable, we obtain $S_{bulk} = (\partial R/\partial\Theta_{ext})(\partial\Theta_{ext}/\partial n)$. The maximum sensitivity is achieved at some angle that corresponds to the sloping edge of the SPR, where reflectivity sharply drops from unity to almost zero. Hence

$$S_{bulk} \approx \frac{1}{\Delta\Theta} \frac{\partial\Theta_{ext}}{\partial n}. \qquad (18)$$

The first factor here is determined by the SPR width [Eqs. (15) and (17)], whereas the second factor $\partial\Theta_{ext}/\partial n$ is a smooth function of the refractive index derived from Eqs. (5) and (7).

To characterize thin dielectric layers with a thickness smaller than the SP penetration depth δ_{zd}, Eq. (12), the SPR sensitivity is defined as follows:[45]

$$S_{layer} = \frac{S_{bulk}}{\delta_{zd}}. \qquad (19)$$

D. IR surface plasmon resonance at the ZnS/Au/water interface: Practical aspects

We will now consider practical aspects of the IR SPR in the water-based samples such as biological specimens. Although SPR at IR frequencies can be excited in many metals,[46] the requirement of biocompatibility leaves gold as the only choice. For the near IR, one can use BK-7 or SF-11 glass prisms, whereas for mid-IR, one can use ZnS or ZnSe prisms.

The range of wavelengths/angles where SPR can be excited is determined by the dielectric losses in water and by the conductive losses in the gold film. Figure 4 shows dielectric losses (upper panel) and the refractive index of water (lower panel). It is clear that SPR at the Au/water interface
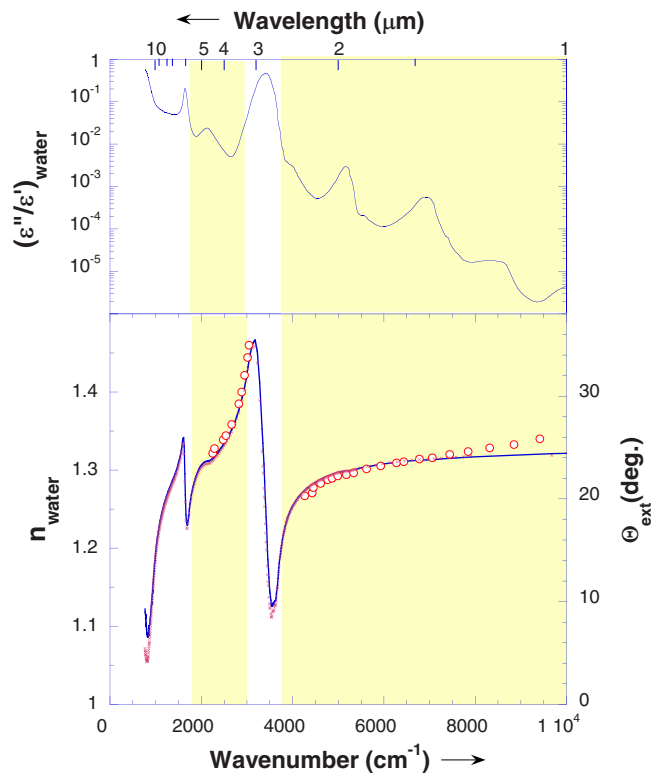
FIG. 4. (Color online) Upper panel: loss tangent of water. The colored areas indicate spectral windows where water absorption is sufficiently low and the SP can be excited. Lower panel: the continuous blue line shows the refractive index of water. Purple crosses denote the SPR angle Θ_{ext} for the ZnS/Au/water interface, as given by Eqs. (5) and (7) (right y-axis). Red circles indicate our experimentally found angles for a 18-nm-thick Au film. The wavelength dependence of the SPR angle mimics the water refractive index.

can be excited only in several "allowed" spectral windows where water absorption is sufficiently low. Figure 4 shows the SPR angle versus the wavelength, as predicted by Eqs. (5) and (7) (lower panel, right y-axis). This dependence mimics the refractive index of water. Note that in the angular interval, $\Theta_{ext} = 20° - 25°$, for each angle there are two SPRs at different wavelengths.

Figure 5 shows SP propagation length L_x as predicted by Eq. (13). This length should be compared to the SP wavelength, $\lambda_{sp} = 2\pi/k'_x$. In the "allowed" spectral ranges, the SP attenuation is low and SP propagates to long distances, $L_x/\lambda_{sp} \gg 1$. In the "forbidden" spectral ranges, the SPR is overdamped and the SP wave quickly attenuates, yielding $L_x/\lambda_{sp} < 1$.

In the context of sensing biological cell cultures, it is useful to compare the SP propagation length L_x to the lateral size of the cell, $d_{cell} \sim 10 - 20 \ \mu m$. In the spectral ranges $\lambda < 1.2 \ \mu m$ and $\lambda > 4.5 \ \mu m$, the SP propagation length is small, $L_x < d_{cell}$, and reflectivity in the SPR regime is the sum of the contributions of individual cells. In the spectral ranges $\lambda_{sp} = 1.2 - 2.6 \ \mu m$ and $\lambda_{sp} \approx 4 \ \mu m$, the SP propagation length is long, $L_x > d_{cell}$; hence, the SP wave senses an "effective medium" consisting of cells and gaps between the cells.

Figure 6 shows the SP penetration depth into a water-based dielectric medium. In the visible and NIR ranges, it is exceedingly small, $\delta_z < 0.24 \ \mu m$. In the context of cell cul-
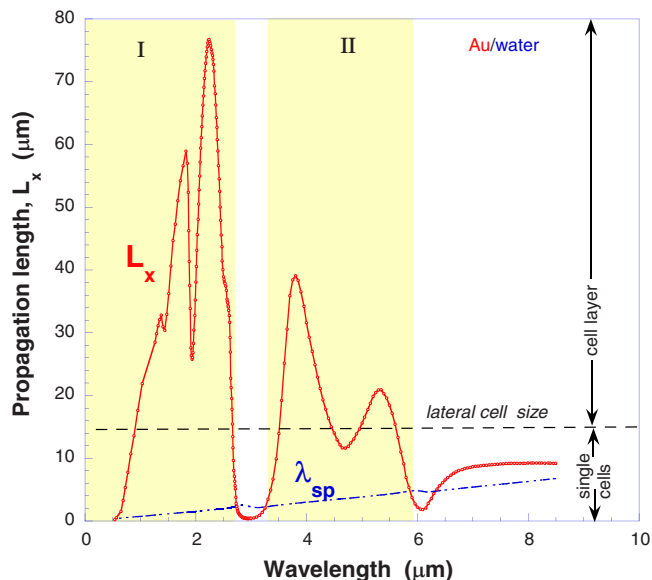

FIG. 5. (Color online) The open circles denote SP propagation length L_x at the ZnS/Au/water interface, as given by Eq. (13) for the optimal Au film thickness. The dash-dotted blue line denotes SP wavelength λ_{sp}. The colored areas indicate spectral windows where SPR can be excited (see Fig. 4). In the "allowed" spectral windows (0.5–3 μm and 3.3–6 μm) $L_x > \lambda_{sp}$, whereas in the "forbidden" windows (3–3.3 μm and above 6 μm), $L_x \leq \lambda_{sp}$. The dashed line denotes lateral cell size. When SP propagates through the cell monolayer grown on gold, it senses either single cells [spectral windows of 0.5–1 μm and 4.5–6 μm, see Fig. 10(e)] or some effective medium consisting of cells and growth solution (spectral windows of 1–2.7 μm and 3.5–4.5 μm).

tures grown on gold, such a small penetration depth is advantageous for studying the cell membrane and cell adhesion. However, a small penetration depth precludes studying the cell interior. In the spectral range $\lambda = 2 - 2.5 \ \mu m$, the SP
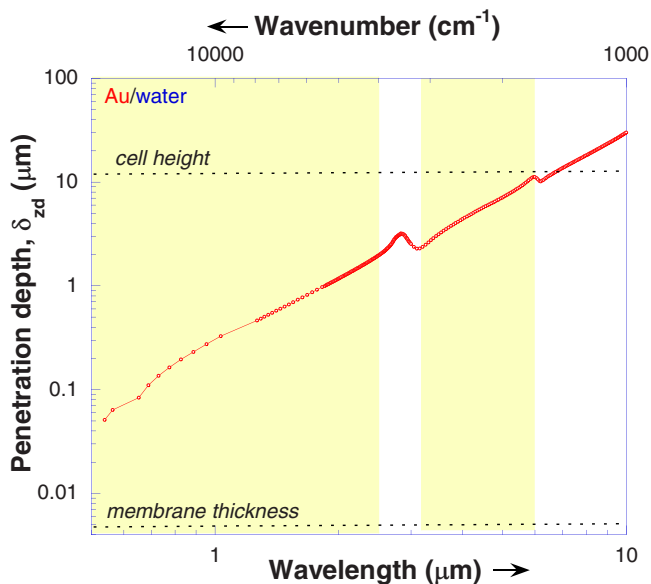

FIG. 6. (Color online) SP penetration depth into biolayer (aqueous solution) as defined by Eq. (12). The colored areas show spectral windows where SPR at the Au-water interface can be excited. In studying cell monolayers, it is important to compare penetration depth (open circles), cell height, and membrane thickness (dashed lines). Penetration of the short-wavelength SP into the cells is strongly limited; hence, it is mostly sensitive to events related to the cell membrane. The long-wavelength SP penetrates deeper into cells and senses the whole cell volume.
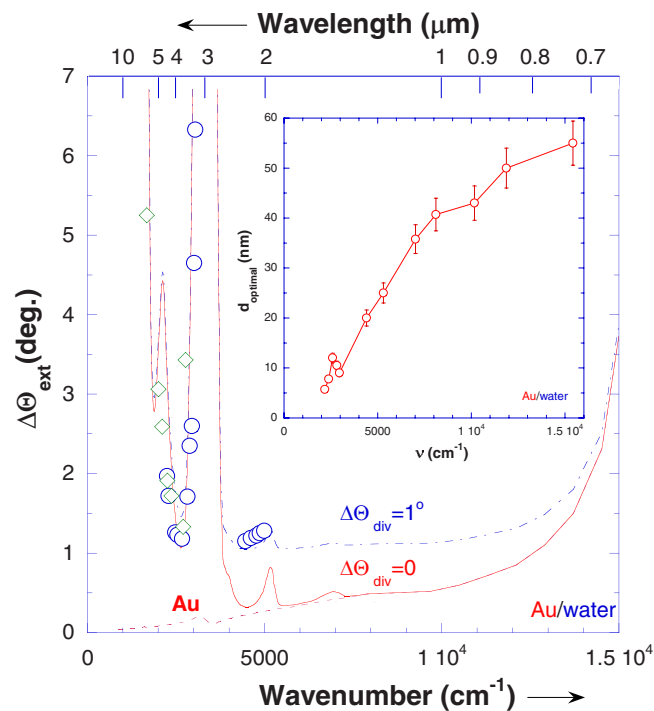
FIG. 7. (Color online) SPR width for the ZnS/Au/water interface. The lines show SPR width, as determined by the absorption in water and in Au and by the coupling (radiation) losses, as predicted by Eq. (16). The continuous red line denotes zero beam divergence and the dash-dotted blue line denotes a beam divergence of 1°. The dashed red line indicates the prediction of Eq. (14), assuming negligible losses in water. Blue circles indicate our experimental results obtained with a 14-nm-thick Au film. The beam divergence was $\Delta\Theta_{div}=0.8°$. In all calculations, we assumed that the Au film thickness is optimal, i.e., it satisfies the critical coupling condition at a given wavelength. The inset shows the optimal Au film thickness that was determined from numerical simulations based on Fresnel reflectivity formulae.

FIG. 8. (Color online) The open circles denote the calculated sensitivity of the SPR technique, $S_{bulk}=\partial R/\partial n$, for different beam divergences, as defined by Eq. (18) and Fig. 4. The lines are the guides to the eye. [Our calculation does not extend into spectral region between 7670 and 9670 cm^{-1} owing to uncertainty in the optical parameters of Au arising from the mismatch between two data sets (Ref. 50).] Sensitivity in mid-IR is higher than that in the visible range.

penetration depth is $\delta_{zd}=1-2$ μm. Hence, the SP wave penetrates deep enough to study events in the cell cytoplasm but not in the nucleus. For the wavelength range $\lambda=4-6$ μm, the penetration depth is comparable to the cell size; hence, the whole cell volume is accessible for the SP.

Figure 7 shows the SPR width versus wavelength, as given by Eqs. (16) and (17). The exact calculation, using the Fresnel reflectivity formulae, yields almost the same results. Note that in the NIR range ($\lambda<1.3$ μm), where water optical absorption is negligible, the SPR width is determined by conductor losses. On the other hand, at $\lambda>2.5$ μm, conductor losses are negligible and the SPR width is determined by water absorption. In the intermediate range, $\lambda=1.3-2.5$ μm, the SPR width achieves its minimum value of 0.3°, whereas the contributions of water absorption and conductor losses are comparable. However, to take full advantage of such a narrow resonance, the incident beam should be very well collimated, otherwise the SPR width in this spectral range would be limited by beam divergence.

The inset in Fig. 7 shows the optimal gold film thickness d required to achieve critical coupling. d decreases with increasing wavelength, in such a way that the operation in mid-IR requires 10–12-nm-thick gold films; this approaches the practical limit at which continuous gold films can be fabricated. When the film thickness deviates from its optimal value, the SPR is excited, although the SPR minimum is not
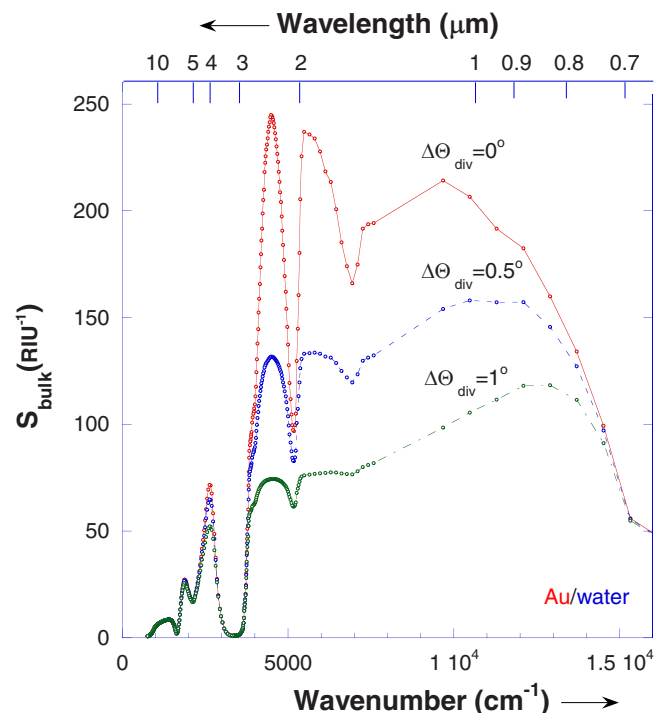
so deep.[1] The symbols in Fig. 7 show our experimental results achieved in two experiments with a 12-nm-thick gold film that was optimized for the operation at $\lambda=5$ μm. At $\lambda>3$ μm, we observe good correspondence between the approximate model and experimental SPR values, whereas at $\lambda<2.5$ μm, the experimental SPR is considerably broadened due to beam divergence and deviation of the film thickness from the optimal value corresponding to this wavelength.

Figure 8 shows the bulk sensitivity of the SPR technique estimated according to Eq. (18). The bulk sensitivity in the IR range is considerably higher than that in the visible range. In the range $\lambda=0.6-2.5$ μm, the sensitivity is more or less constant, whereas in the long-wavelength window, $\lambda=3.3-5$ μm, it is lower but is still comparable to that in the visible range. This means that both these spectral windows may be used for SPR spectroscopy.

Figure 9 shows the thin layer sensitivity. The maximum sensitivity is achieved in NIR at $\lambda=800$ nm, whereas the sensitivity in the mid-IR is lower. Hence, the NIR range is especially advantageous for studying thin dielectric films on gold substrate.

E. Surface plasmon propagation in biological samples

We consider several regimes in which the FTIR-SPR technique can be used to study biological objects. These objects (cell membrane, single cell, cell culture, etc.) have different sizes and the SP propagation there is also different.
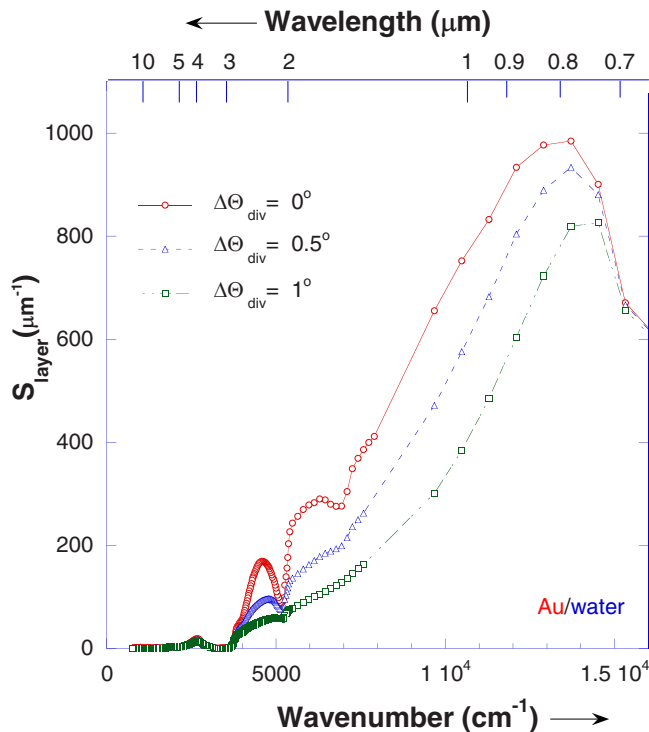
FIG. 9. (Color online) Sensitivity of the SPR technique to a thin layer with thickness much smaller than the SP penetration depth, as defined by Eq. (19). The number at each curve indicates beam divergence. The maximum sensitivity is achieved for $\lambda \sim 0.8$ μm.

Indeed, the SP propagation depends on the relation between the spatial extent of the SP wave and the characteristic size of the sample. Hence, by selecting the proper wavelength, the SPR can be made especially sensitive to the processes occurring at a targeted spatial scale. Figure 10 illustrates several regimes of SP sensing.

- [Figs. 10(a) and 10(b)] Thick and macroscopically uniform biolayers. Here, SP probes the bulk refractive index of the biolayer. This can be used for monitoring biologically important molecules in solutions, for example, glucose. An interesting modification is a suspension of floating cells, for example, erythrocytes.
- [Fig. 10(c)] A very thin biolayer attached to the gold film, for example, a membrane, or biomolecular recognition layer with a thickness of only 1–5 nm. Although the SP penetration depth usually exceeds this thickness, the short-wavelength SP is sensitive enough to characterize them.
- [Fig. 10(d)] A moderately thick biolayer with thickness comparable to the wavelength. Here, in addition to the SP wave, additional waveguide modes can appear. These can be useful for depth-resolved biosensing and for probing cell adhesion and cell-cell attachment.
- [Figs. 10(e) and 10(f)] Cell cultures grown directly on metal. Here, depending on the propagation length, the SP wave can probe either individual cells or the cell layer as a whole.

III. EXPERIMENTAL

Next, we will present several biological applications of the FTIR-SPR technique. Figure 11 shows our experimental
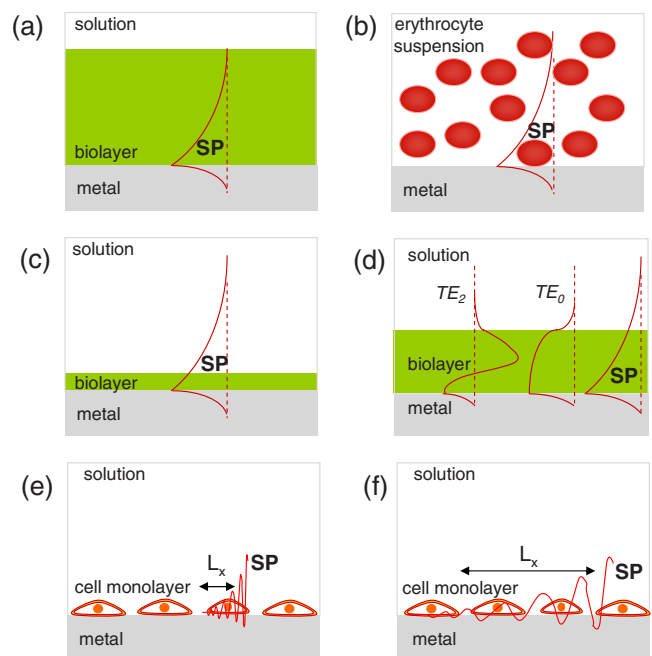

FIG. 10. (Color online) SP propagation in biological samples. (a) Thick biolayer (solution or bulk sample). SP decays within this layer and is not sensitive to anything beyond it. (b) Cell suspension, for example, erythrocytes. SP partially or fully penetrates into cells that are close to the metal. SP can be used to study these cells provided the SP penetration depth is comparable to the cell size. (c) A very thin biolayer in contact with metal (membrane, adsorbed molecules). To study such thin layers, the SP penetration depth should be short enough. (d) A biolayer of intermediate thickness in contact with metal. Here, in addition to the exponentially decaying SP wave, the guided modes can be excited as well. These waveguide modes have sinusoidal field distribution inside the layer and may be advantageous for layer characterization. (e) Cell culture grown on metal. The SP propagation length is smaller than the lateral cell size. The reflectivity in the SPR regime represents a sum of the contributions of individual cells. (f) SP propagation length exceeds lateral cell size. The SP probes an "effective medium" consisting of cells and extracellular space.

setup based on the Bruker Equinox 55 FTIR spectrometer. The light source is a tungsten lamp equipped with the KBr beam splitter. The IR beam is emitted from the external port of the spectrometer and passes through a collimator consisting of a pinhole mounted at the common focal plane of two Au-coated off-axis parabolic mirrors with a focal length of 76.2 and 25.4 mm, correspondingly. For the 1-mm-diameter pinhole, the beam diameter is 3–4 mm and the beam divergence is $\Delta\Theta_{div} = 0.8°$. The collimated beam passes through the grid polarizer (Specac, Ltd.) and is reflected from the right-angle ZnS prism (ISP Optics, Inc.) mounted on a Θ-2Θ rotating table. Another parabolic mirror focuses the reflected beam on the liquid-nitrogen-cooled HgCdTe (MCT) detector. A temperature-stabilized flow chamber (with a volume of 0.5 ml) is in contact with the gold-coated base of the prism. The gold film thickness is chosen according to the targeted wavelength (Fig. 7, inset).

To operate this setup, we first choose the desired incident angle. Then we mount the sample and measure the reflectivity spectrum for the *s*-polarized beam. This spectrum is used as a background for further measurements. Then we measure the reflectivity spectrum for the *p*-polarized beam. Normally, this is done with 4 cm^{-1} resolution and 16 scan averaging.
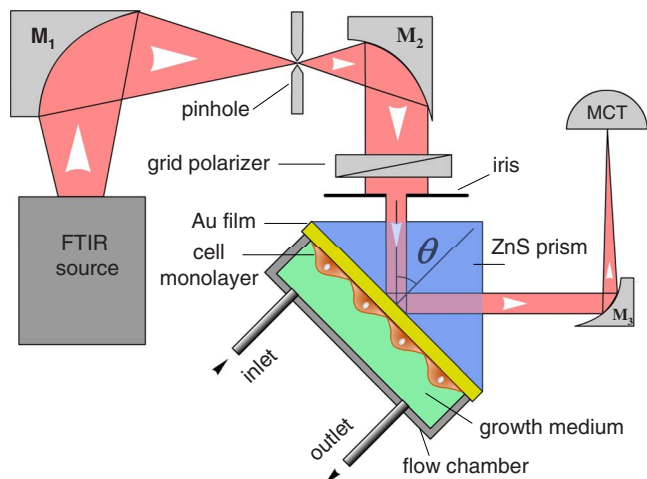
FIG. 11. (Color online) The FTIR-SPR setup. The IR beam from the FTIR spectrometer is collimated by two parabolic mirrors, M1 and M2, and a pinhole. The collimated beam is polarized by the grid polarizer, it passes through the ZnS prism, and is reflected from its base. The reflected beam is focused by the parabolic mirror, M3, on the MCT detector. The base of the prism is Au-coated and it is in contact with the flow chamber. The samples can be of two kinds: (i) a biosolution in the flow chamber or (ii) a biological membrane or cell monolayer grown directly on the base of the Au-coated prism. In the latter case, the flow chamber is filled with growth medium.

A. Solutions

1. Glucose concentration in water

We used the FTIR-SPR technique for precisely measuring the refractive index of solutions. Our motivation was to monitor physiologically important glucose concentrations in water and in human plasma.[43] Similar studies have been performed earlier using SPR in the visible range.[47–49] Figure 12 shows the reflectivity spectra of pure water and of 1% D-glucose solution measured using our setup. The spectral range around 4000 cm^{-1} corresponds to the short-wavelength SPR and the small peak at 2000 cm^{-1} corresponds to the long-wavelength SPR. Adding glucose affects the whole reflectivity spectrum, in such a way that the SPR resonance is redshifted. The maximal reflectivity change occurs at 4600 cm^{-1}. The inset shows that the reflectivity at 4600 cm^{-1} linearly increases with increasing glucose concentration. The slope of this linear dependence yields sensitivity, $S_{bulk} = \partial R / \partial n = 75$ RIU^{-1}. Taking into account the actual beam divergence of 0.8°, the experimental sensitivity is consistent with the approximate expression given by Eq. (18) (see also Fig. 8).

2. Glucose uptake by erythrocytes

Here we studied glucose uptake by erythrocyte suspension in the PBS medium.[51] Briefly, fresh human red blood cells (RBCs) were washed four times in PBS by centrifugation. The supernatant and buffy coat cells were discarded and RBCs were resuspended in glucose-free PBS to yield c_e =5% v/v. For complete glucose depletion, cells were incubated for 60 min at 22 °C in PBS. Then, RBCs were centrifuged and resuspended in fresh PBS containing the required concentrations of D-glucose supplemented with L-glucose to
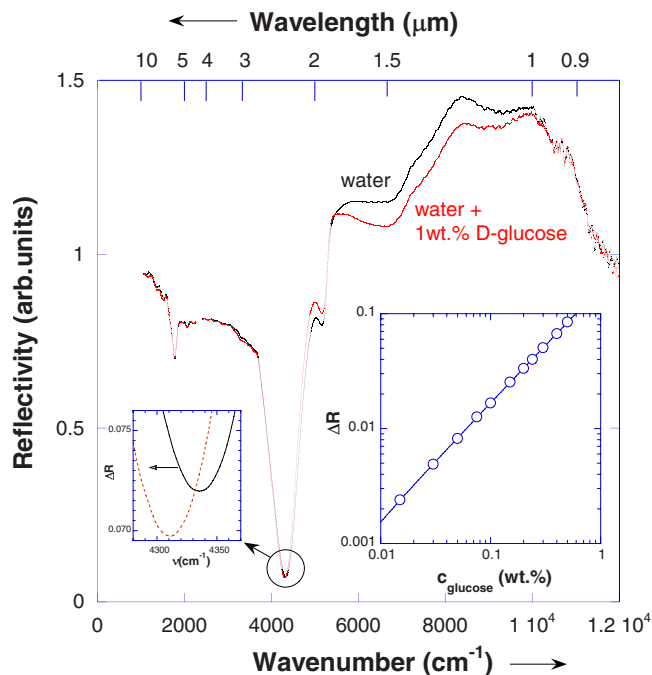

FIG. 12. (Color online) Reflectivity from the ZnS/Au/water interface (black dots). The gold film thickness is 13 nm and the incident angle is $\Theta_{ext}=21°$. The red dots denote the corresponding results for 1 wt % of D-glucose water solution. The SPR for the Au/water interface is manifested by a pronounced dip at 4334 cm^{-1}. Addition of 1 wt % of D-glucose shifts this dip to 4310 cm^{-1}. A secondary dip at 1780 cm^{-1} is a long-wavelength SP; the features at 5145 cm^{-1} and at 6900 cm^{-1} indicate the water absorption peaks. The inset shows that ΔR at 4600 cm^{-1} (this wave number corresponds to the slope of the SPR and the reflectivity here is extremely sensitive to slight variations in the refractive index) linearly depends on the D-glucose concentration. The slope of this linear dependence yields a bulk sensitivity, $S_{bulk}=dR/dn=75$ RIU^{-1}.

keep the total glucose concentration (osmolarity) equal to 20 mM. The SPR measurements were performed at 22 °C to slow down cellular glycolysis.

Our measurements were performed using a ZnS prism coated with a 12 nm thick Au film. We chose the wavelength $\lambda=4$ μm at which the SP penetration depth, $\delta_{zd}=4.5$ μm (Fig. 6), is comparable to the typical erythrocyte diameter. Although the sensitivity at this wavelength is low (Fig. 8), the use of such a long wavelength here is mandatory in order to sense the processes inside erythrocytes. The average distance between the erythrocytes is $\sim D_e c_e^{1/3}=17$ μm. The SP propagation length, $L_x=30$ μm (Fig. 5), exceeds the distance between erythrocytes. Hence, in the "coherence area" of the SP wave, $(\delta_{zd}L_x)$, there are one to two erythrocytes.

The erythrocytes intensively absorb D-glucose, which affects their refraction index and probably their shape. The optical reflectivity from the erythrocyte suspension changes correspondingly. Indeed, Fig. 13 shows that, upon addition of D-glucose, reflectivity in the SPR regime rapidly increases with time until saturation occurs. The rate of this process increases when cells are exposed to higher glucose concentrations.

In another experiment, cells were exposed to a solution containing 20 mM D-glucose supplemented with 20 μM of the GLUT-1 inhibitor, cytochalasin B (CB). A negligible reflectivity change was observed in the presence of the inhibi-
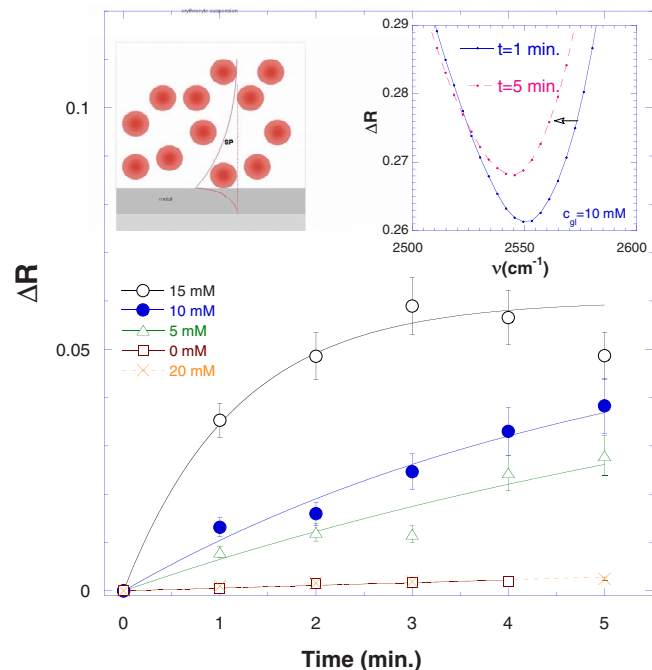
FIG. 13. (Color online) Glucose uptake by erythrocyte suspension. We used here a long-wavelength SP at $\lambda \approx 4$ μm and a 12-nm-thick Au film in order to achieve a sufficiently high penetration depth, $\delta_{zd}=4.5$ μm, which is comparable to the typical erythrocyte diameter. The left-hand inset schematically shows SP penetration into erythrocytes. The right-hand inset shows the SPR reflectivity from the erythrocyte suspension before and after exposure to 10 mM of D-glucose. The SPR minimum shifts with time to longer wavelengths (redshift), indicating glucose uptake by erythrocytes. The open symbols in the main panel indicate SPR reflectivity change (at a fixed wavelength) for erythrocyte suspension in the PBS buffer with different concentrations of D-glucose. Upon addition of D-glucose, ΔR increases and achieves saturation. Continuous lines indicate exponential fit $\Delta R \propto (1 - e^{-\alpha t})$, whereas the rate α increases with glucose concentration. The orange crosses indicate the results of another experiment where cells were exposed to solution containing 20 mM D-glucose supplemented with 20 μM of the GLUT-1 inhibitor, CB. As expected, a negligible reflectivity variation was observed in the presence of the inhibitor.
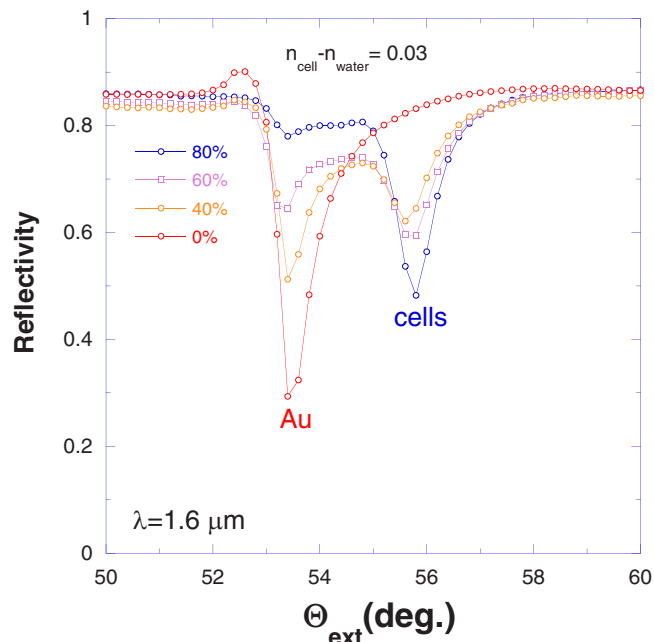

FIG. 14. (Color online) Angular dependence of the SPR from the HeLa cell monolayers with different cell coverage (confluence). We used here an SF-11 right-angle glass prism coated with a 35-nm-thick Au film. In the absence of cells, there is a single SPR minimum at $\Theta_{ext}=53.4°$, which corresponds to the reflectivity from the ZnS/Au/water interface. In the presence of cells, an additional SPR dip appears at $55.8°$, which corresponds to the reflectivity from the ZnS/Au/cells interface. The angular shift between these two minima yields the refractive index difference, $n_{cell}-n_{water}=0.03$. At high cell confluence (80%), the SPR signal from the cells is dominant.

tor. Similarly, minor changes in the reflectivity were detected when cells were exposed to a plain buffer solution. We interpret these results as follows: the erythrocytes absorb D-glucose (but not L-glucose) and this affects their refractive index. Although the exact mechanism by which the SP wave interacts with the erythrocytes is not yet clear, we believe that the observed SPR variation is associated with D-glucose uptake by erythrocytes because (i) the rate of SPR change is determined by the glucose concentration and (ii) the SPR change is inhibited by CB, as expected. Therefore, we can conclude that FTIR-SPR measurements specifically sense a glucose-dependent transport process. This conjecture is corroborated by the dielectric spectroscopy measurements on similar suspensions.[52]

B. Cell culture studied by the SPR: The physics involved

We succeeded in growing cell cultures directly on the Au-coated prism.[42,44] These include human melanoma (MEL 1106), MDCK, and HeLa cells that form monolayers with a typical confluence of 60%–80%. In a typical experiment, the prism with a cell culture was removed from the incubator,

attached to a flow chamber, mounted in the FTIR-SPR setup, and then exposed to HEPES buffered medium (MEM) at 37 °C. The temperature in the flow chamber was controlled within 0.1 °C while the buffer solution was constantly pushed through the chamber at a flow rate of 5 μl/min using a motorized bee syringe pump. After 5–7 min of equilibration, we measured the reflectivity in the SPR regime. The measurements lasted up to 6 h, after which, the cells usually die, most probably from the lack of CO_2.

1. Surface plasmon propagation in the cell culture

Understanding SP propagation in the cell monolayer necessitates further discussion. Indeed, the cells have irregular shapes with a lateral size of $\sim 10 \times 20$ μm^2 and a height of 1 to 6 μm. Since the cells contain up to 25% organic molecules, their average refractive index exceeds that of water. This results in an angular shift of the SPR resonance [Eq. (5)] for the ZnS/Au/cell interface, compared to the ZnS/Au/water interface. However, even at high cell confluence, some parts of the Au-coated prism can be uncovered by cells. These Au patches may exhibit an unshifted SPR, provided their size exceeds the SP propagation length, $l_{patch}>L_x$.

Figure 14 summarizes our studies of the HeLa cell monolayers grown on an SF-11 gold-coated glass prism. Here we used a relatively short wavelength $\lambda=1.6$ μm. The corresponding penetration depth is also small, $\delta_{zd}=0.7$ μm (Fig. 6) but sufficient to probe the cell's interior. The propagation length, $L_x=46$ μm (Fig. 5), exceeds the average cell size. Figure 14 shows angular-dependent reflectivity for dif-
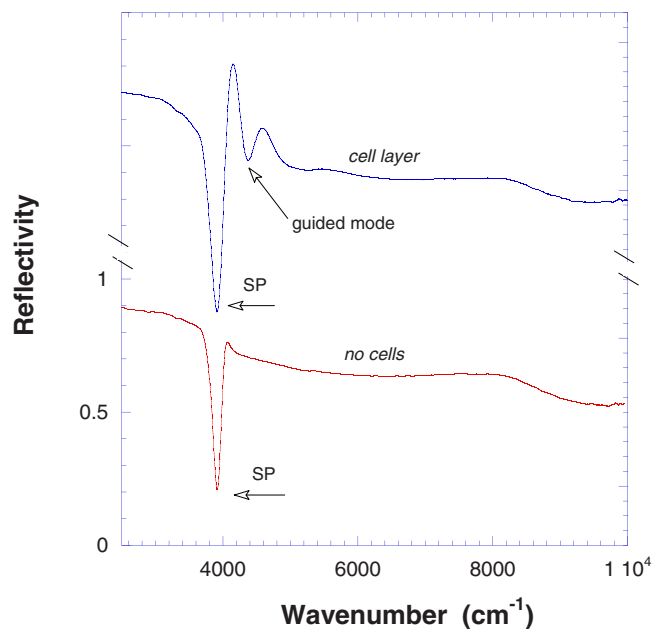
FIG. 15. (Color online) Reflectivity in the SPR regime for a melanoma 1106-cell culture in MEM growth solution (upper curve, $\Theta = 19.5°$) and growth solution without cells (lower curve, $\Theta = 18.6°$). The upper curve is displaced upwards for clarity. Note the main SPR dip at 3920 cm^{-1} in both curves and a satellite dip at 4385 cm^{-1} in the upper curve. We associate this dip with the TE$_0$ waveguide mode propagating in the cell monolayer.

ferent cell coverages (confluences). In the absence of cells, there is a single dip at $\Theta_{sp} = 53.4°$ that corresponds to the SPR at the ZnS/Au/water interface. In the presence of HeLa cells, an additional dip appears at $\Theta_{sp} = 55.8°$, which corresponds to the ZnS/Au/HeLa cell interface. The SPR angular shift corresponds to $n_{cell} - n_{water} = 0.03$. For high cell confluence, e.g., 80%, the SPR from uncovered gold patches is barely seen, as expected.

2. Guided modes

Since the refractive index of cells exceeds that of the surrounding aqueous medium ($n_{cell} > n_{water}$) and the cell monolayer thickness is comparable to the mid-IR wavelength ($d_{cell} \sim \lambda$), the cell monolayer on gold could behave as a metal-clad optical waveguide.[53] An indication of such behavior is seen in Fig. 15, which shows an SPR spectra (i) for a human MEL 1106 cell monolayer grown on an Au-coated ZnS prism at high confluence and (ii) for the similar Au-coated prism without cells. In both cases, there is a strong SPR at 3920 cm^{-1} ($\lambda = 2.55$ μm). For the prism with cell culture, a short-wavelength satellite appears at 4385 cm^{-1} ($\lambda = 2.28$ μm). We associate this feature with the waveguide mode propagating in the cell monolayer [Fig. 10(d)].

Indeed, the cutoff condition for the TE and TM modes in the planar metal-clad dielectric waveguide is[3,53]

$$k_0 d_{cell} \sqrt{n_{cell}^2 - n_{water}^2} = \left(m + \tfrac{1}{2}\right)\pi, \qquad (20)$$

where $m = 0, 1, 2 \cdots$. We substitute here $n_{water} = 1.25$, $n_{cell} - n_{water} = 0.03$, $d_{cell} = 2$ μm; for the lowest TE$_0$ mode we found that $\lambda_0 = 2.3$ μm ($\nu = 4348$ cm^{-1}). This estimate corresponds fairly well to our observation shown in Fig. 15.
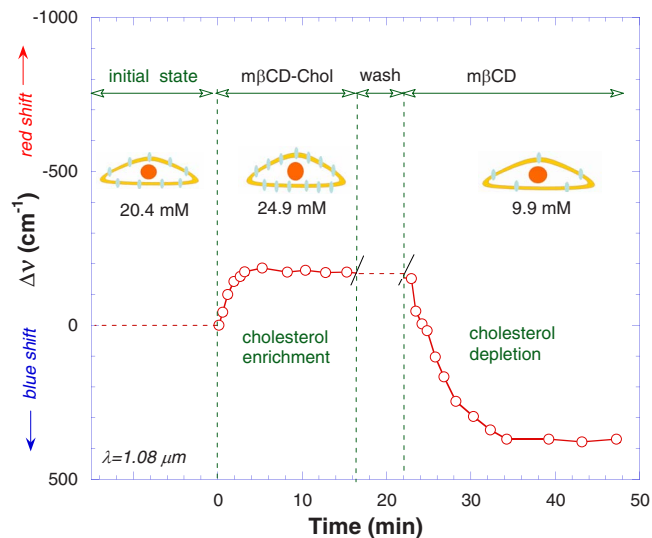

FIG. 16. (Color online) SPR shift upon cholesterol enrichment/depletion of HeLa cell membranes. The drawings show cholesterol molecules in the cell membrane (gray ovals); the numbers below the drawings indicate cholesterol concentration in the membrane, as was determined biochemically on analogous cell cultures. In order to be sensitive to membrane-related processes, the SPR measurements were performed at a short wavelength, $\lambda = 1.08$ μm, to ensure short penetration depth, $\delta_{zd} = 0.36$ μm (see Fig. 6). At $t = 0$ we injected 10 μM of mβCD-chol solution. The SPR becomes red-shifted, as expected, since the accumulation of cholesterol molecules with a high refractive index in the cell membrane increases the average refractive index. At $t = 15$ min, the cells were washed with plain medium for 5 min and then 3 μM mβCD solution was added. The SPR became blueshifted since this drug depletes cell membranes from cholesterol in such a way that the average refractive index in the SPR-sensed region decreases.

Note that the SP propagation length at this wavelength is very long, $L_x = 73$ μm (Fig. 5), as expected.

C. Cell cultures studied by the SPR technique: The biology involved

1. Cholesterol in the cell membrane

We studied cholesterol penetration into the plasma membrane of the HeLa cells[42] using our FTIR-SPR technique (similar studies using SPR in the visible range were performed in Ref. 54). It is well-known that cholesterol from the extracellular solution enters mostly into the plasma membrane rather than into cytoplasm. Therefore, to achieve high sensitivity to membrane-related events, we chose the NIR wavelength range, $\lambda_{sp} = 1 - 1.08$ μm, characterized by a relatively low SPR penetration depth.

The HeLa cells were grown on an SF-11 glass prism coated with a 35-nm-thick gold film. The prism with cells was mounted into a flow chamber and was equilibrated in growth medium for 5–7 min at 37 °C. Then, we added 10 mM of mβCD-chol (methyl-beta-cyclodextrin loaded with cholesterol), which is known to enrich the cells with cholesterol.

We measured the FTIR-SPR spectra before and after adding the drugs. Figure 16 shows that after exposure to mβCD-chol the SPR is redshifted. This corresponds to a refractive index increase because cholesterol has a higher refractive index than water. In contrast, when we add to a growth solution a similar chemical, mβCD, which is not loaded with cholesterol, the SPR is blueshifted, which corre-
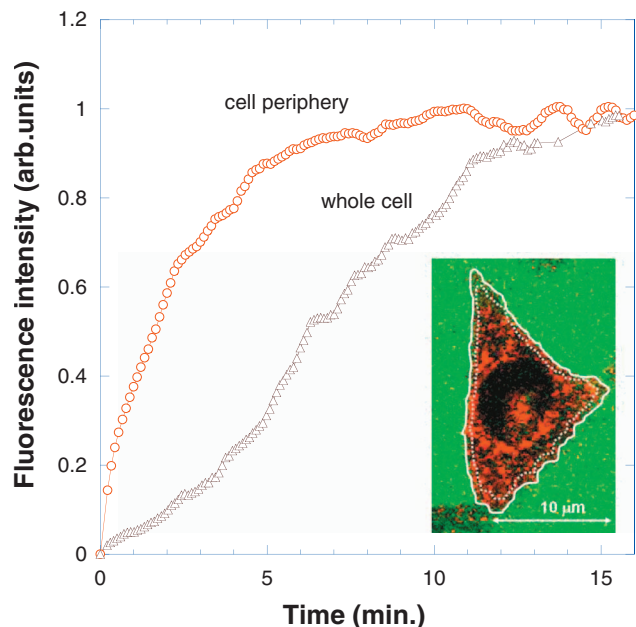
FIG. 17. (Color) Cell fluorescence resulting from the rhodamine-tagged ferrotransferrin (Tfn) penetration into cells. The red circles represent the peripheral region of the cell, whereas the green triangles denote the fluorescence from the whole cell. Note the fast fluorescence kinetics in the peripheral regions of the cell, as compared with the slow kinetics in the whole cell. The inset shows the confocal microscope image of a single cell under partial penetration of the ferrotransferrin.
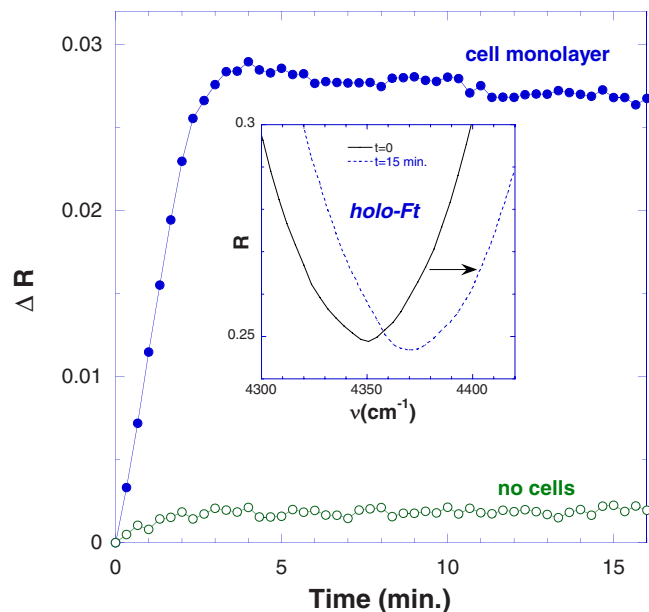

FIG. 18. (Color online) Reflectivity variation in the SPR regime following the introduction of holo-ferrotransferrin. The open circles indicate the results for the ZnS/Au/growth solution interface when there is no cell culture. Here, introduction of the holo-Ft does not result in significant changes in reflectivity, indicating negligible holo-Ft adsorption on the Au surface. The filled circles indicate a holo-Ft-induced reflectivity change from the ZnS/Au/Mel 1006/water interface. There is pronounced SPR reflectivity change that closely follows the kinetics of fluorescence from the peripheral parts of the cells. The inset shows that the SPR in this case is blueshifted.

sponds to a refractive index decrease. This is expected since mβCD depletes plasma membranes from cholesterol. Consistent with this explanation, the SPR reflectivity in the cholesterol-depleted state is lower than the initial SPR reflectivity.

2. Ferrotransferrin uptake

We applied our FTIR-SPR technique to study transferrin-induced clathrin-mediated endocytic processes that introduce Fe ions into the cell. Figure 17 shows a fluorescence image of a melanoma 1106 cell obtained by confocal microscopy.[55] The inset shows the cell interior in black, the red areas indicate Fe penetration, and the green areas indicate extracellular space. It is clearly seen that the fluorescence intensity increases and then achieves saturation, whereas its kinetics in the peripheral part of the cell is faster than that in the whole cell.

We studied the same process using a long-wavelength SP at $\lambda = 2.54$ μm. Its penetration depth, $\delta_{zd} = 1.2$ μm (Fig. 6), is long enough to penetrate the cells, although it senses mostly the cell periphery. Figure 18 shows SPR reflectivity variation upon introduction of Tfn into the solution. The kinetics of the SPR reflectivity closely follows the fluorescence kinetics in the cell periphery (Fig. 17), as expected. This example demonstrates that the SPR results are consistent with the confocal microscopy observations using fluorescent tags. The obvious advantage of the SPR technique is that it is label-free.

Interestingly, the SPR here is blueshifted, indicating that the average refractive index in the measured volume decreases (Fig. 18, inset). This rules out the possibility that the SPR shift results from accumulation of organic molecules in

the cell (this would increase the refractive index). The blueshift indicates that the cells become "diluted," as if the growth solution penetrates into cells. This could be explained by formation of endocytic vesicles.

IV. DISCUSSION AND CONCLUSIONS

The conclusions are as follows:

- In the context of biosensing, the lack of convenient laser sources and the enhanced water absorption were considered as major impediments for extending the SPR technique into the mid-IR range. We demonstrated here that there are several spectral windows, where by a clever choice of wavelength, beam collimation, angle of incidence, and metal film thickness, the SPR technique can achieve sensitivity that is comparable and even higher than that in the visible range.
- SPR in mid-IR can be used to study cells and cell cultures. This technique is well matched for the sensing of cells since the SP penetration depth in the IR range is just on the order of the cell size. This is in contrast with the SP in the visible range, whose penetration depth is too short to probe the processes inside the cell cytoplasm. However, to develop the FTIR-SPR technique into a useful tool for studying cells, one must theoretically analyze SP propagation and scattering in a cell monolayer.
- The waveguide modes in cell culture may develop into a useful tool to study cell-cell attachment and cell adhesion to substrates.
- The most challenging task in the field of FTIR-SPR is

to convert it into a spectroscopic tool that allows measuring the FTIR absorption/dispersion spectra in the regime of the SPR. The sensitivity of this technique should surpass that of FTIR-ATR (Ref. 56) and allow detection of biomolecules according to their fingerprints.

[1]H. Raether, *Surface plasmons on smooth and rough surfaces and on coatings* (Springer, Berlin, 1988).
[2]S. A. Maier, *Plasmonics: Applications and Fundamentals* (Springer, New York, 2007).
[3]W. Knoll, Annu. Rev. Phys. Chem. **49**, 569 (1998).
[4]S. A. Maier and H. A. Atwater, J. Appl. Phys. **98**, 011101 (2005).
[5]G. Gauglitz, G. Proll, Biosensing for the 21 century **109**, 395 (2008).
[6]J. Homola, S. S. Yee, and G. Gauglitz, Sens. Actuators B **54**, 3 (1999).
[7]J. Homola, Anal. Bioanal. Chem. **377**, 528 (2003).
[8]J. Homola, Chem. Rev. (Washington, D.C.) **108**, 462 (2008).
[9]K. S. Phillips and Q. Cheng, Anal. Bioanal. Chem. **387**, 1831 (2007).
[10]R. L. Rich and D. G. Myszka, Curr. Opin. Biotechnol. **11**, 54 (2000).
[11]A. J. Haes and R. P. Van Duyne, Anal. Bioanal. Chem. **379**, 920 (2004).
[12]R. Ince and R. Narayanaswamy, Anal. Chim. Acta **569**, 1 (2006).
[13]X. D. Hoa, A. G. Kirk, and M. Tabrizian, Biosens. Bioelectron. **23**, 151 (2007).
[14]R. J. Green, R. A. Frazier, K. M. Shakeshe, M. C. Davies, C. J. Roberts, and S. J. B. Tendler, Biomaterials **21**, 1823 (2000).
[15]I. D. Alves, C. K. Park, and V. J. Hruby, Curr. Protein Pept. Sci. **6**, 293 (2005).
[16]M. Besenicar, P. Macek, J. H. Lakey, and G. Anderluh, Chem. Phys. Lipids **141**, 169 (2006).
[17]A. Dahlin, M. Zach, T. Rindzevicius, M. Kall, D. S. Sutherland, and F. Hook, J. Am. Chem. Soc. **127**, 5043 (2005).
[18]P. Pattnaik, Appl. Biochem. Biotechnol. **126**, 79 (2005).
[19]Z. Salamon, H. A. Macleod, and G. Tollin, Biochim. Biophys. Acta **1331**, 117 (1997).
[20]Z. Salamon, G. Lindblom, and G. Tollin, Biophys. J. **84**, 1796 (2003).
[21]M. P. Jonsson, P. Jonsson, A. B. Dahlin, and F. Hook, Nano Lett. **7**, 3462 (2007).
[22]K. Morigaki and K. Tawa, Biophys. J. **91**, 1380 (2006).
[23]Y. Fang, A. M. Ferrie, N. H. Fontaine, J. Mauro, and J. Balakrishnan, Biophys. J. **91**, 1925 (2006).
[24]K. F. Giebel, C. Bechinger, S. Herminghaus, M. Riedel, P. Leiderer, U. Weiland, and M. Bastmeyer, Biophys. J. **76**, 509 (1999).
[25]M. Hide, T. Tsutsui, H. Sato, T. Nishimura, K. Morimoto, S. Yamamoto, and K. Yoshizato, Anal. Biochem. **302**, 28 (2002).
[26]Y. Yanase, H. Suzuki, T. Tsutsui, I. Uechi, T. Hiragun, S. Mihara, and M.
Hide, Biosens. Bioelectron. **22**, 1081 (2007).
[27]T. Liebermann and W. Knoll, Colloids Surf., A **171**, 115 (2000).
[28]J. M. Brockman, B. P. Nelson, and R. M. Corn, Annu. Rev. Phys. Chem. **51**, 41 (2000).
[29]A. A. Kolomenskii, P. D. Gershon, and H. A. Schuessler, Appl. Opt. **39**, 3314 (2000).
[30]M. Zangeneh, N. Doan, E. Sambriski, and R. H. Terrill, Appl. Spectrosc. **58**, 10 (2004).
[31]Z.-M. Qi, M. Wei, H. Matsuda, I. Honma, and H. Zhou, Appl. Phys. Lett. **90**, 181112 (2007).
[32]J. V. Coe, K. R. Rodriguez, S. Teeters-Kennedy, K. Cilwa, J. Heer, H. Tian, and S. M. Williams, J. Phys. Chem. **111**, 17459 (2007).
[33]G. Brink, H. Sigl, and E. Sackmann, Sens. Actuators B **25**, 756 (1995).
[34]A. Ikehata, X. L. Li, T. Itoh, Y. Ozaki, and J. H. Jiang, Appl. Phys. Lett. **83**, 2232 (2003).
[35]A. Ikehata, T. Itoh, and Y. Ozaki, Anal. Chem. **76**, 6461 (2004).
[36]J. F. Masson, Y. C. Kim, A. Loius, L. A. Obando, W. Peng, and K. S. Booksch, Appl. Spectrosc. **60**, 1241 (2006).
[37]S. Patskovsky, A. V. Kabashin, M. Meunier, and J. H. T. Luong, J. Opt. Soc. Am. A Opt. Image Sci. Vis. **20**, 1644 (2003).
[38]S. Patskovsky, A. V. Kabashin, M. Meunier, and J. H. T. Luong, Sens. Actuators B **97**, 409 (2004).
[39]A. G. Frutos, S. C. Weibel, and R. M. Corn, Anal. Chem. **71**, 3935 (1999).
[40]B. P. Nelson, A. G. Frutos, J. M. Brockman, and R. M. Corn, Anal. Chem. **71**, 3928 (1999).
[41]V. Lirtsman, R. Ziblat, M. Golosovsky, D. Davidov, R. Pogreb, V. Sacks-Granek, and J. Rishpon, J. Appl. Phys. **98**, 093506 (2005).
[42]R. Ziblat, V. Lirtsman, D. Davidov, and B. Aroeti, Biophys. J. **90**, 2592 (2006).
[43]V. Lirtsman, M. Golosovsky, and D. Davidov, J. Appl. Phys. **103**, 014702 (2008).
[44]V. Yashunsky, S. Shimron, V. Lirtsman, A. M. Weiss, N. Melamed-Book, M. Golosovsky, D. Davidov, and B. Aroeti, Biophys. J. (unpublished).
[45]K. Johansen, H. Arwin, I. Lundstrom, and B. Liedberg, Rev. Sci. Instrum. **71**, 3530 (2000).
[46]G. W. Bradberry and J. R. Sambles, Opt. Commun. **67**, 404 (1988).
[47]W. W. Lam, L. H. Chu, and C. L. Wong, Sens. Actuators B **105**, 138 (2005).
[48]K. Aslan, J. R. Lakowicz, and C. D. Geddes, Anal. Chem. **77**, 2007 (2005).
[49]H. V. Hsieh, Z. A. Pfeiffer, T. J. Amiss, D. B. Sherman, and J. Bruce Pitner, Biosens. Bioelectron. **19**, 653 (2004).
[50]E. D. Palik, *Handbook of Optical Constants of Solids II* (Academic, New York, 1991).
[51]The phosphate-buffered saline buffer (PBS) has a pH of 7.4 and contains 137 nM NaCl, 8.9 mM Na_2HPO_4, 2.7 mM KCl, 1.5 mM KH_2PO_4. We used (from healthy donors) fresh human erythrocytes that were washed in PBS and centrifugated three times for 5 min at $300 \times g$. The washed erythrocytes were suspended in the PBS and stored in ice.
[52]Y. Hayashi, L. Lifshitz, A. Caduff, and Y. Feldman, J. Phys. D **36**, 369 (2003).
[53]A. Yariv and P. Yeh, *Optical Waves in Crystals* (Wiley, New York, 1984), p. 473.
[54]M. P. Besenicar, A. Bavdek, A. Kladnik, P. Macek, and G. Anderluh, Biochim. Biophys. Acta **1778**, 175 (2008).
[55]The cells were imaged with an Olympus FV-1000 confocal microscope, equipped with an on-scope incubator (Life Image Services). The holo-Ft was tagged with rhodamine red.
[56]K. K. Chittur, Biomaterials **19**, 357 (1998).